

Detecting precursors for an imminent landslide along the Jinsha River

Wentao Yang¹, Lianyou Liu^{2,3,4}, Peijun Shi^{2,3,4}

¹Three-gorges Reservoir Area (Chongqing) Forest Ecosystem Research Station, School of Soil and Water Conservation, Beijing Forestry University, Beijing, 100083, China

5 ²Academy of Disaster Reduction and Emergency Management, Ministry of Emergency Management & Ministry of Education, Beijing Normal University, Beijing, 100875, China

³MOE, Key Laboratory of Environmental Change and Natural Disaster, Beijing Normal University, Beijing, 100875, China

⁴State Key Laboratory of Earth Surface Processes and Resource Ecology, Beijing Normal University, Beijing, 100875, China

Correspondence to: Lianyou Liu (lyliu@bnu.edu.cn) and Peijun Shi (spj@bnu.edu.cn)

10 **Abstract.** Landslides are major hazards that may pose serious threats to mountain communities. Even landslides in remote mountains could have non-negligible impacts on populous regions by blocking large rivers and forming dam-breached mega floods. Usually, there are slope deformations before major landslides occur, and detecting precursors such as slope movement before major landslides is important for preventing possible disasters. In this work, we applied multi-temporal optical remote sensing images (Landsat 7 and Sentinel-2) and an image correlation method to detect sub-pixel slope deformations of a slope
15 near the Mindu town in the Tibet Autonomous Region. This slope is located on the right bank of the Jinsha River, ~80km downstream the famous Baige landslide. We used a DEM derived aspect to restrain background noises in image correlation results. We found the slope remained stable from November 2015 to November 2018 and moved significantly since November 2018. We used more data to analyse slope movement in 2019 and found retrogressive slope movements with increasingly large deformations near the river bank. We also analysed spatial-temporal patterns of the slope deformation from October 2018 to
20 February 2020 and found seasonal variations in slope deformations. Only the foot of the slope moved in dry seasons, whereas the entire slope activated in rainy seasons. Until 24 August 2019, the size of the slope with displacements larger than 3 m is similar to that of the Baige landslide. However, the river width at the foot of this slope is much narrower than the river width at the foot of the Baige landslide. We speculate it may continue to slide down and threaten the Jinsha River. Further modelling works should be done to check if the imminent landslide could dam the Jinsha River and measures be taken to mitigate possible
25 dammed breach flood disasters. This work illustrates the potential of using optical remote sensing to monitor slope deformations over remote mountain regions.

1 Introduction

Landslides are major natural hazards in mountain regions and have been causing widespread disasters every year around the globe (Petley 2012; Zhang et al. 2020). Major landslides in remote mountain regions may pose serious threats to
30 downstream communities by choking channels to increase the risks of landslide-dammed lake outburst floods (Fan et al. 2020; Liu et al. 2019). For example, a hillslope near the Baige village had two landslides, damming the Jinsha River twice in 2018.

The outburst floods caused widespread damage along its route and affected as far as Yunnan Province, > 500km from the landslides (Fan et al. 2019). In 2000, a super-large landslide dammed the Yigong River in Tibet and two months later the outburst flood caused widespread damages, including 5 main bridges, highways and communication cables in downstream areas (Shang et al. 2013). The breach of the 1786 landslide-dammed lake in the Dadu river consumed >100,000 lives along its route (Dai et al. 2005). Similar cases could occur in many mountain regions in the world and detecting precursors (such as slope movement) before major landslides is crucial for preventing such disasters (Intrieri et al. 2018; Carlà et al. 2019).

Remote sensing techniques have been an efficient way to monitor slope movement over large mountain regions (Du et al. 2020; Handwerger et al. 2019). Optical passive and radar remote sensing are most frequently used data to detect slope displacements. There are two kinds of mainstream methods to derive slope movement. SAR interferometry processing use the difference in phase images to derive subtle slope movement of a few millimetres (Intrieri et al. 2018; Samsonov et al. 2020). However, large ground displacements (e.g., a few metres), dense vegetation or long time intervals could lead to incoherence in phase images in this type of methods (Wasowski and Bovenga 2014). Image correlation methods (also referred as the pixel offset tracking used in SAR intensity images) is another type of methods that use SAR amplitude or optical images to correlate image patches to measure slope movement, which can derive sub-pixel ground displacements from 1/10 ~ 1/30 of a pixel (Li et al. 2020). The later type is good at detecting larger slope movements that are visible on images (Bradley et al. 2019; Lacroix et al. 2020). In recent years, image correlation methods have been proposed and widely used to detect sub-pixel slope displacements in optical images (Bontemps et al. 2018; Lacroix et al. 2019; Lacroix et al. 2018; Yang et al. 2020).

In this work, using sub-pixel optical image correlation methods we report a landslide along the Jinsha River. Different from previous retrospective studies, the landslide in this work did not collapse yet. We used multi-temporal Sentinel-2 images and found the slope is unstable and could pose a threat to downstream areas by blocking the Jinsha River.

2 Methods

2.1 Study Area

The reported slope is ~80 km downstream the Baige landslide (Fan et al. 2019) along the Jinsha River near the Mindu town, Tibet Autonomous Region, bordering Sichuan Province (Figure 1a). The slope is located on the right bank of the Jinsha River. Similar to the Baige landslide, the geomorphology of this section of the Jinsha River is at the bottom of V-shaped valley. The elevation of the study area ranges from 2660m at the valley bottom to >4500m on the mountain ridge. This rough topography indicates strong fluvial incision against the rapid uplift of the Tibetan Plateau. We estimated the mean annual precipitation (MAP) by using the GPM v6 monthly precipitation (from 2001 to 2019) and found the MAP of this area is ~665mm. The region is controlled by monsoon climate with >90% of the rain occurring from May to October.

This area is tectonically active and active faults run through this slope from north to south. To the west of the faults are Upper Paleozoic strata, and to the east are Mesoproterozoic metamorphic rocks. Cracks and fissures on the slope is visible from the 15 m resolution pan-sharpened false colour Landsat 7 image acquired in 2001 (Figure 1b). These cracks and fissures

may be relics of historic earthquakes or precipitations. This part of the slope has a percent slope of 45% and an aspect of the
65 southeast, with azimuth between 112.5° and 157.5° (Figure 1c). The slope is mainly covered by grass and sparse shrubs and
less affected by anthropogenic activities. Field reconnaissance is not carried out for this slope due to outbreak of the COVID-
19 pandemic. Instead, we examined the slope via Google Earth images. Fissure cracks is clearly visible on uppermost part of
the slope, and there are widespread cracks on the lower part of the slope. Evidenced by very high spatial resolution Google
Earth images, the landslide in this work is a translational type (Highland and Bobrowsky 2013).

70 In this work, we mainly relied on Sentinel-2 optical images to derive slope movement. The European Space Agency's
Sentinel-2 mission has two twin satellites in orbit, with a revisit time of less than 5 days. The Sentinel-2 optical imagery has
12 optical bands with wavelength ranging from 440nm to 2200nm (Gascon et al. 2017). There are 4 bands with a spatial
resolution of 10m: blue, green, red and near infrared bands. To derive slope movement, we used the red band because its
wavelength is longer than other visible bands and is less influenced by the atmosphere. Compared to the near infrared, this
75 band is less sensitive to vegetation and is more reliable to measure slope deformation (Yang et al. 2019). We used the Level-
1C product, which is already orthorectified before distribution (Gascon et al. 2017).

2.2 The COSI-Corr method

This work used the COSI-Corr method, a correlation method for optical images to detect slope displacements
(Leprince et al. 2007). To derive slope movement, two images in a roll should be used to form an image pair, including the
80 base image and the target image. The base image is an earlier image, based on which image correlation algorithm (here we use
the COSI-Corr) is implemented to detect slope displacements in the target image (Leprince, et al. 2007). For detailed
parameters to use the COSI-Corr method, please refer to Yang, et al. (2019b).

In this work, we used three steps to detect slope displacements for the studied Mindu slope. For the first step, we used
two image pairs (#1-#2) to find the stable and moving periods before and after November 2018. For the second step, we used
85 19 images in the stable period to estimate cumulative slope displacements in 5 target images in the moving period (image pair
#3-#97). For the third step, we used another nine images to derive displacements for every two adjacent images (image pair
#98-#105).

2.2.1 Deriving slope displacements

In the first step, we used three Sentinel-2 images (on 13 November 2015, 12 November 2018 and 12 November 2019)
90 to compose two image pairs (#1 and #2). The first image pair (#1) is composed of a Sentinel-2 image on 13 November 2015
and a Sentinel-2 image on 12 November 2018. Sentinel-2 images of the second pair (#2) are acquired on 12 November 2018
and on 12 November 2019.

By using the first two image pairs, we found the slope was stable from 13 November 2015 to 12 November 2018 and
moved significantly from 12 November 2018 to 12 November 2019. Therefore, in the second step, we used two image groups,
95 a base image group in the stable period and a target image group in the moving period, to detect cumulative slope displacements

(Table 1). For the base image group, there are 19 clear images without clouds in 2018. For the target image group, we selected five images in 2019 (13 April, 17 July, 24 August, 5 October and 12 November) to detect cumulative displacements. In all, there are 19×5 image pairs (#3-#97) calculated in the second step. In the third step, we used nine images from 28 September 2018 to 7 February 2020 (Table 2) to form another eight image pairs (#98-#105) to derive slope displacements.

100 2.2.2 Error Assessment and postprocessing

Misalignments between images can be estimated by selecting a stable zone (Bontemps et al. 2018; Lacroix et al. 2018; Yang et al. 2019). In this work, the stable zone was selected on the upper part of the landslide (red rectangular in Fig 1b and 1c). Mean displacements estimated within the stable zone were used to correct image shifts. Standard deviations of the displacements within the stable zone represents uncertainties, indicating the quality of the derived results for a given image pair. We selected this area because this stable zone is on the same slope as the landslide, which can minimize the influence of illumination and orthorectification errors.

In this work, we cross-validated measured slope displacements for five target images in 2019 in the second step. Uncertainties of the slope displacements for a given target image were estimated from all 19 base images in the stable periods. Standard deviations of these 19 measurements were used to indicate their reliability. We further filtered out displacements with moving directions that does not agree with the SRTM DEM derived aspects. If there are 15° deviations between the derived slope movement and the aspect, the derived slope movement is defined as invalid and will not be used for further analysis.

3 Results

3.1 Detected stable and unstable periods

115 In Table 3, the EW-mean and NS-mean indicate the east-west (EW) and north-south (NS) shifts of images in both image pairs calculated from the stable zone. The EW-std and NS-std are standard deviations of displacements in the stable zone to indicate image distortions. Low EW-std and NS-std values indicates good performances during image orthorectifications. The derived EW-mean and NS-mean were used to correct misalignments in image pairs.

The base and target images for image pair #1 are on 13 November 2015 and 12 November 2018, respectively. The base and target images for image pair #2 are on 12 November 2018 and 12 November 2019, respectively. The slope remains stable in the first image pair, whereas detectable slope displacements can be found in the second image pair (Figure 2). The durations of image pair #1 and pair #2 span 3 years and one year, respectively. In Figure 2a, we can see that the slope displacement from 2015 to 2018 was less than 2 m, whereas there was >6 m slope displacement from 2018 to 2019 (Figure 2b). In image pair #2, larger displacements were observed near the Jinsha River and smaller displacements were farther away from the river. This increasing displacement magnitude indicate the slope may start to move from its toe.

3.2 Cumulative slope displacements in 2019

As in Figure 2, we can see that this slope remained stable from November 2015 to November 2018 and moved after November 2018. To derive time series of the Mindu slope displacements after November 2018, we used 19 base images in the stable period and 5 target images in 2019. All 19 base images are from early 2018, during which the slope was stable. Five
130 selected target images are acquired on 13 April 2019, 17 July 2019, 24 August 2019, 5 October 2019 and 12 November 2019. For each target image in 2019, we calculated slope movement by using all base images. Therefore, there are 19 estimated slope displacements for each target image. We calculated the means and standard deviations of slope displacements for all target images (Figure 3).

From Figure 3, we can see that the mean displacements are a magnitude larger than standard deviations, which
135 indicate that the displacements derived between each target image and their base images agree with each other quite well. Minor slope displacements were detected until April 2019 (maximum 3~4m), whereas larger slope displacements can be observed in the later four target images (>5 m). All displacements in five target images show a similar pattern with results in image pair 2 (Figure 2b), demonstrated by larger displacements near the river and less movement further from the river.

We further selected six points on the slope to analyse time series of the slope displacements in 2019 (Figure 4). For
140 most target images in the first five points (p1-p5), most base images could derive >10 valid displacements (2-D columns). For all six points, accumulated displacements show similar growing trends from April 2019 to November 2019. Maximum displacements in all six points occurred on 24 August 2019. These unreasonably large values may be caused by difference of solar elevation/zenith angles in target images. For example, compared to the August image there are more mountain shadows in the November images in northern hemisphere. Despite abnormal displacements in August 2019, we can still see that
145 displacements from July to November 2019 are still larger than displacements in April 2019. Therefore, from time series of these six points, we can see that major slope displacements occurred from April to August 2019.

3.3 Slope displacements in eight selected periods after November 2018

To analyse spatial deformation patterns in different periods, we selected 9 Sentinel-2 images forming eight image
pairs (image pair #98-#105 in Table 2, corresponding to eight periods in ~2 months). The first two image pairs (Figure 5a-b,
150 #98 and #99) shows that the middle and lower parts of the slope deformed significantly and 4-6 meters of displacement occurred at multiple locations. The study area has a monsoonal climate with most precipitation occurs from May to September (Figure 6). There are seasonal differences in deformation of this landslide. In dry seasons of winter and spring, deformation occurs at the foot of the slope near the Jinsha River and deformation rate is generally less than 1 m/month (from January to May, Figure 5c&d and periods 3-4 in Figure 6, image pairs #100-#101). In rainy seasons of summer and autumn, deformation
155 affects the entire slope with some parts at a rate of more than 3 meters/month (from May to September, Figure 5e&f and periods 5-6 in Figure 6, image pair #102-#103).

4 Discussion

4.1 Possible impacts of this imminent landslide

Major landslides in mountains may dam river channels forming transient lakes, the breach of which can result in catastrophic floods to downstream communities (Dai et al. 2005; Fan et al. 2019; Liu et al. 2019). In this work, we examined a hillslope near the Mindu town along the Jinsha River. We found the slope had significant movement from November 2018 to November 2019. Despite the area of the detected moving slope (715,577 m² for displacements larger than 3 m) is similar with the area of the Biage landslide (830,624 m²), the width of the Jinsha River channel below the Mindu slope (~ 50) is half that of the Baige (>100 m, in Figure 7). Considering the similar morphology of both river sections, the collapse of the Mindu slope could pose a threat to downstream communities by blocking the Jinsha River. We call for further frequent monitoring of the hillslope in combination with other tools, such as InSAR (Intrieri et al. 2018; Samsonov et al. 2020).

4.2 Comparison of image matching and InSAR methods

In this work, we used the COSI-Corr method to derive slope displacements for the Mindu slope along the Jinsha River. The principle of this method is to use a sliding window to find pattern matches to derive displacements in image pairs (Leprince et al. 2007). Compared to the InSAR methods, this method is easier to understand and implement. In addition, image correlation methods favour larger displacements than InSAR methods. Limited by the wavelength of SAR image, InSAR methods are versed in monitoring ground deformation of millimetre to centimetre scale (Intrieri et al. 2018), whereas the capability of image correlation methods depends on spatial resolution of images. In general, image correlation methods are more reliable for deriving large ground displacements of metre scale (Bradley et al. 2019; Lacroix et al. 2020). In this work, it might be quite challenging for InSAR methods to detect such large displacements.

Long temporal intervals of a few months could lead to incoherence in SAR images (Li et al. 2019), whereas images (taken on the same season) with long temporal intervals of a few years can be used to derive reliable displacements given a stable land cover (Yang 2020). Both methods can be affected by the atmosphere. Clear optical images without clouds should be used in image correlation methods. Although SAR images could penetrate thin clouds, atmosphere could cause phase delay and lead to uncertainties in derived results (Li et al. 2019).

Both methods works well on bare land without vegetation, though dense vegetation could seriously affect InSAR methods (Intrieri et al. 2018). On the contrary, image correlation methods are less affected by vegetation cover as long as images in the pair are from the same season (Yang 2020). As image correlation methods use pattern matches within an image pair, we speculate that vegetation density may not be a major challenge for the method. The Sentinel-2 images used in this work have four 10-metre resolution optical bands (Gascon et al. 2017). In theory, any of these four bands may be used to derive slope displacements. But, an ideal band should not be sensitive to ground cover change unrelated with ground displacements, which could minimize background noises. In general, optical bands with shorter wavelength is more prone to

be affected by moisture in the atmosphere. Considering that near infrared band is very sensitive to vegetation, we used the red band in this work.

190 Both InSAR and image correlation methods can be impacted by complex terrains in mountain regions. Layover and shadow areas in SAR images should not be used in InSAR methods (Li et al. 2019). Similarly, shadows in optical images also influence derived results (Yang et al. 2020). To derive reliable results, optical images acquired during larger solar angles should be prioritized to minimize the influence of mountain shadows. Fortunately, there are algorithms developed to restore information in mountain shadows in optical images (Shahtahmassebi et al. 2013), which may promote the efficacy of optical
195 image correlation methods.

4.3 Measures taken to reduce uncertainties

Many other factors may also influence the accuracy of slope deformation from image correlation methods, which includes image orthorectification errors, different viewing angles during image acquisition, different illuminations in images, et al. (Stumpf et al. 2016; Yang et al. 2020). This work used the Sentinel-2 L1C product, which is already orthorectified before
200 distribution (Gascon et al. 2017). To correct for possible mis-registration between the base and target images, we used a stable zone to calculate and correct image shifts. To reduce errors caused by different illuminations, all images used for the first two Sentinel-2 image pairs are from similar dates of different years.

The first two image pairs (#1 and #2) we mentioned above are composed of images of very similar acquire dates in different years. Images of similar dates have similar zenith/elevation angles, which could minimize the influence of mountain
205 shadows (Yang et al. 2020). To assess and reduce uncertainties in the second step, we first identified a stable period. Then, we used 19 base images in this stable period to derive cumulative displacements for a given target image in the moving period. The mean displacements from these 19 image pairs are expected to be more reliable than results from a single image pair. In addition, these 19 measurements can cross-validate each other and be used to estimate uncertainties by standard deviations (Figure 3 and Figure 4).

210 There are a few strategies to suppress background noises in derived results, including selecting results with high signal/noise ratios (Lacroix et al. 2018; Yang et al. 2020), integrating redundant information in time series of images (Bontemps et al. 2018). This work introduced a simple and efficient way by using slope aspect to filter out slope movement that is different from the aspect. This is reasonable for this translational landslide as the mass moves downhill driven by gravity. This procedure could eliminate false slope movements and reserve true slope movement of the Mindu landslide. By integrating topographic
215 information, this new procedure is expected to work well for ground movement in other regions that is consistent with slope configurations.

4.4 Potential applications of the method in landslide monitoring

As we used orthorectified images, slope displacements derived in this work are horizontal movements. To derive ground movement along the slope, we need to consider local slope configurations. Because image correlation methods use

220 sliding windows to detect similar patterns between the base and target images, precursors with horizontal rather than vertical ground movements can be detected. Landslides that have intact moving surfaces can be detectable by image correlation methods. For translational and rotational landslides, there are more horizontal than vertical ground movements, which are ideal landslide types to use image correlation methods, whereas precursors of avalanches, rock falls may be difficult to detect due to limited horizontal ground movement (Highland and Bobrowsky 2013).

225 In addition, the smallest displacements that can be detected depends on the spatial resolution of optical images (Li et al. 2020, Stumpf et al. 2016). Although image correlation methods can detect sub-pixel ground movement, it is very challenging to detect moving surfaces that cover an area of a few pixels, as smaller window sizes could result in more background noises (Yang et al. 2020).

5 Conclusions

230 In this work, by using the COSI-Corr method and multi-temporal Sentinel-2 images, we found precursors of a major landslide along the Jinsha River in southwest China. Fissures on the slope probably existed before 2001 but the slope remained stable between November 2015 and November 2018. From November 2018 to August 2019, we detected significant slope displacements. The size of the activated part on the Mindu slope is similar to that of the 2018 Baige landslide, whereas the river width under the Mindu slope is half of the Baige section. If this landslide continues to slide down and fails completely, 235 it may block the Jinsha River leading to similar consequences as the Baige landslide.

By using image correlation technique, we can track sub-pixel slope movement in optical remote sensing images. We also adopted an aspect constraint to pick out downslope movement and significantly depressed background noises. However, optical images, such as the Sentinel-2 images, can only detect slope movements up to a few metres. To continuously monitor this slope, other data and methods (such as higher spatial resolution data or InSAR techniques) should be used. We also call 240 for intensive monitoring of this slope and modelling of landslides caused river blocking and subsequent flooding.

Data availability. All Sentinel-2 images and the Landsat 8 image in this work were downloaded from the GEE. The SRTM DEM and its derivative were downloaded from the Geospatial Data Cloud website (<http://www.gscloud.cn/sources>).

Supplement. There is no related supplement for this paper.

245 Author contribution. LL and PS discovered the moving slope of this work. WY conducted analysis and drafted the manuscript. Competing interests. The authors declare no conflict of interest.

Acknowledgement. WY would like to show his gratitude to his large family for catering his 2-year old daughter, while this work was underway.

Financial support. This work is jointly supported by the National Science Foundation of China (No. 41807500) and the Second 250 Tibetan Plateau Scientific Expedition and Research Program (STEP), Grant No. 2019QZKK0902.

References

- Bontemps, N., Lacroix, P., and Doin, M.-P.: Inversion of deformation fields time-series from optical images, and application to the long term kinematics of slow-moving landslides in Peru. *Remote Sens. Environ.*, 210, 144-158, <https://doi.org/10.1016/j.rse.2018.02.023>, 2018.
- 255 Bradley, K., Mallick, R., Andikagumi, H., Hubbard, J., Meilianda, E., Switzer, A., Du, N., Brocard, G., Alfian, D., Benazir, B., Feng, G., Yun, S.-H., Majewski, J., Wei, S., and Hill, E.M.: Earthquake-triggered 2018 Palu Valley landslides enabled by wet rice cultivation. *Nat. Geosci.*, 12, 935-939, <https://doi.org/10.1038/s41561-019-0444-1>, 2019.
- Carlà, T., Intrieri, E., Raspini, F., Bardi, F., Farina, P., Ferretti, A., Colombo, D., Novali, F., and Casagli, N.: Perspectives on the prediction of catastrophic slope failures from satellite InSAR. *Scientific Report*, 9, 14137, <https://doi.org/10.1038/s41598-019-50792-y>, 2019.
- 260 Dai, F., Lee, C., Deng, J., and Tham, L.G.: The 1786 earthquake-triggered landslide dam and subsequent dam-break flood on the Dadu River, southwestern China. *Geomorphology*, 65, 205-221, <https://doi.org/10.1016/j.geomorph.2004.08.011>, 2005.
- Du, J., Glade, T., Woldai, T., Chai, B., and Zeng, B.: Landslide susceptibility assessment based on an incomplete landslide inventory in the Jilong Valley, Tibet, Chinese Himalayas. *Eng. Geol.*, 270, 105572, <https://doi.org/10.1016/j.enggeo.2020.105572>, 2020.
- 265 Fan, X., Dufresne, A., Subramanian, S.S., Strom, A., Hermanns, R., Stefanelli, C.T., Hewitt, K., Yunus, A.P., Dunning, S., Capra, L., Geertsema, M., Miller, B., Casagli, N., Jansen, J.D., and Xu, Q.: The formation and impact of landslide dams – State of the art. *Earth-Science Reviews*, 203, 103116, <https://doi.org/10.1016/j.earscirev.2020.103116>, 2020.
- Fan, X., Xu, Q., Alonso-Rodriguez, A., Subramanian, S.S., Li, W., Zheng, G., Dong, X., and Huang, R.: Successive landsliding and damming of the Jinsha River in eastern Tibet, China: prime investigation, early warning, and emergency response. *Landslides*, 16, 1003-1020, <https://doi.org/10.1007/s10346-019-01159-x>, 2019.
- 270 Gascon, F., Bouzinac, C., Thépaut, O., Jung, M., Francesconi, B., Louis, J., Lonjou, V., Lafrance, B., Massera, S., Gaudel-Vacaresse, A., Languille, F., Alhammoud, B., Viallefont, F., Pflug, B., Bieniarz, J., Clerc, S., Pessiot, L., Trémas, T., Cadau, E., De Bonis, R., Isola, C., Martimort, P., and Fernandez, V.: Copernicus Sentinel-2A Calibration and Products Validation Status. *Remote Sens.*, 9(6), 584, <https://doi.org/10.3390/rs9060584>, 2017.
- Handwerker, A.L., Fielding, E.J., Huang, M., Bennett, G.L., Liang, C., Schulz, W.H.: Widespread Initiation, Reactivation, and Acceleration of Landslides in the Northern California Coast Ranges due to Extreme Rainfall. *J. Geophys Res-Earth*, 124, 1782-1797, <https://doi.org/10.1029/2019JF005035>, 2019.
- Highland, L. and Bobrowsky, P.: *The Landslide Handbook—a Guide to Understanding Landslides: A Landmark Publication for Landslide Education and Preparedness*. Springer Berlin Heidelberg. 2013.
- 280 Intrieri, E., Raspini, F., Fumagalli, A., Lu, P., Del Conte, S., Farina, P., Allievi, J., Ferretti, A., and Casagli, N.: The Maoxian landslide as seen from space: detecting precursors of failure with Sentinel-1 data. *Landslides*, 15, 123-133, <https://doi.org/10.1007/s10346-017-0915-7>, 2018.

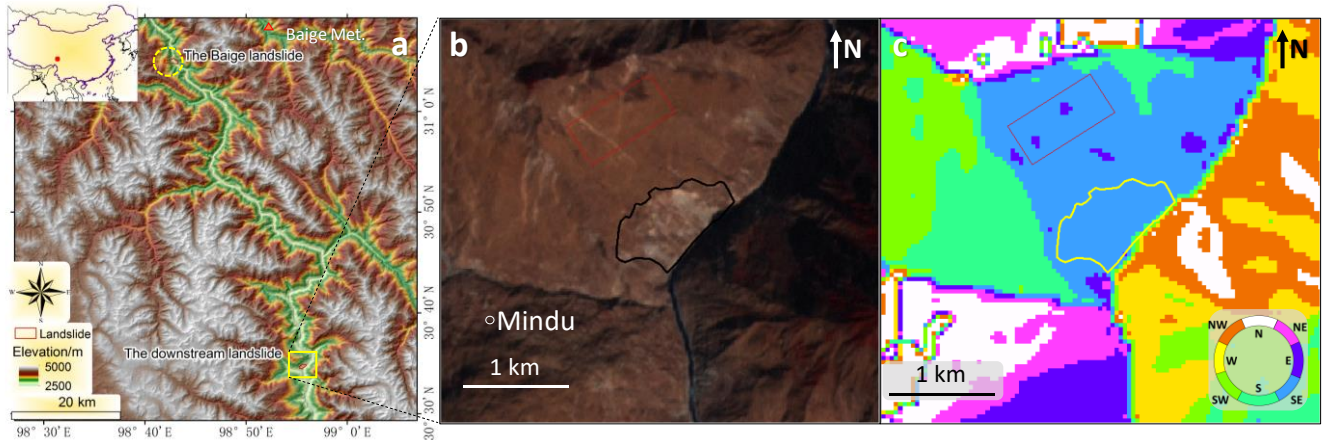
- Lacroix, P., Araujo, G., Hollingsworth, J., and Taïpe, E.: Self-Entrainment Motion of a Slow-Moving Landslide Inferred From Landsat-8 Time Series. *J. Geophys Res-Earth*, 124, 1201-1216, <https://doi.org/10.1029/2018jf004920>, 2019.
- Lacroix, P., Berthier, E., and Maquerhua, E.T.: Earthquake-driven acceleration of slow-moving landslides in the Colca valley, Peru, detected from Pléiades images. *Remote Sens. Environ.*, 165, 148-158, <https://doi.org/10.1016/j.rse.2015.05.010>, 2015.
- Lacroix, P., Bièvre, G., Pathier, E., Kniess, U., and Jongmans, D.: Use of Sentinel-2 images for the detection of precursory motions before landslide failures. *Remote Sens. Environ.*, 215, 507-516, <https://doi.org/10.1016/j.rse.2018.03.042>, 2018.
- 285 Lacroix, P., Dehecq, A., and Taïpe, E.: Irrigation-triggered landslides in a Peruvian desert caused by modern intensive farming. *Nat. Geosci.*, 13, 56-60, <https://doi.org/10.1038/s41561-019-0500-x>, 2020.
- Leprince, S., Barbot, S., Ayoub, F., and Avouac, J.: Automatic and Precise Orthorectification, Coregistration, and Subpixel Correlation of Satellite Images, Application to Ground Deformation Measurements. *IEEE T. Geosci. Remote*, 45, 1529-1558, <https://doi.org/10.1109/TGRS.2006.888937>, 2007.
- 295 Li, M., Zhang, L., Ding, C., Li, W., Luo, H., Liao, M., and Xu, Q.: Retrieval of historical surface displacements of the Baige landslide from time-series SAR observations for retrospective analysis of the collapse event. *Remote Sens. Environ.*, 240, 111695, <https://doi.org/10.1016/j.rse.2020.111695>, 2020.
- Li, Z., Song, C., Yu, C., Xiao, R., Chen, L., Luo, H., Dai, K., Ge, D., Ding, Y., Zhang, Y., Zhang, Q.: Application of satellite radar remote sensing to landslide detection and monitoring: challenges and solutions. *Geomatics and Information Science of Wuhan University*, 44(7): 967-979, <http://dx.doi.org/10.13203/j.whugis20190098>, 2019.
- 300 Liu, W., Carling, P., Hu, K., Wang, H., Zhou, Z., Zhou, L., Liu, D., Lai, Z., and Zhang, X.: Outburst floods in China: A review. *Earth-Science Reviews*, 197, 102895, <https://doi.org/10.1016/j.earscirev.2019.102895>, 2019.
- Luo, S., Jin, X. and Huang, D.: Long-term coupled effects of hydrological factors on kinematic responses of a reactivated landslide in the Three Gorges Reservoir. *Eng. Geol.*, 261, 105271, <https://doi.org/10.1016/j.enggeo.2019.105271>, 2019.
- 305 Petley, D.: Global patterns of loss of life from landslides. *Geology*, 40, 927-930, <https://doi.org/10.1130/G33217.1>, 2012.
- Samsonov, S., Dille, A., Dewitte, O., Kervyn, F., and d'Oreye, N.: Satellite interferometry for mapping surface deformation time series in one, two and three dimensions: A new method illustrated on a slow-moving landslide. *Eng. Geol.*, 266, 105471, <https://doi.org/10.1016/j.enggeo.2019.105471>, 2020.
- Shahtahmassebi, A., Yang, N., Wang, K., Moore, N., and Shen, Z.: Review of shadow detection and de-shadowing methods in remote sensing. *Chin. Geogr. Sci.* 23, 403-420, <https://doi.org/10.1007/s11769-013-0613-x>, 2013.
- Shang, Y., Yang, Z., Li, L., Liu, D., Liao, Q., and Wang, Y.: A super-large landslide in Tibet in 2000: background, occurrence, disaster, and origin. *Geomorphology*, 54(3-4), 225-243, [https://doi.org/10.1016/S0169-555X\(02\)00358-6](https://doi.org/10.1016/S0169-555X(02)00358-6), 2003.
- Stumpf, A., Malet, J.P., Puissant, A., and Travelletti, J.: Monitoring of Earth Surface Motion and Geomorphologic Processes by Optical Image Correlation. *Land Surface Remote Sensing*, 147-190, <https://doi.org/10.1016/B978-1-78548-105-5.50005-0>, 2016.
- 315 Wasowski, J. and Bovenga, F.: Investigating landslides and unstable slopes with satellite Multi Temporal Interferometry: Current issues and future perspectives. *Eng. Geol.*, 174, 103-138, <https://doi.org/10.1016/j.enggeo.2014.03.003>, 2014.

Yang, W., Wang, Y., Sun, S., Wang, Y., and Ma, C.: Using Sentinel-2 time series to detect slope movement before the Jinsha River landslide. *Landslides*, 16, 1313-1324, doi: 10.1007/s10346-019-01178-8, 2019.

320 Yang, W., Wang, Y., Wang, Y., Ma, C., and Ma, Y.: Retrospective deformation of the Baige landslide using optical remote sensing images. *Landslides*, 17, 659-668, <https://doi.org/10.1007/s10346-019-01311-7>, 2020.

Zhang, S., Li, C., Zhang, L., Peng, M., Zhan, L., and Xu, Q.: Quantification of human vulnerability to earthquake-induced landslides using Bayesian network. *Eng. Geol.*, 265, 105436, <https://doi.org/10.1016/j.enggeo.2019.105436>, 2020.

325



330

Figure 1: Topographic maps of the study area. (a) Geographic locations of the Baige landslide and the downstream landslide around the Mindu town, Tibet Autonomous Region. (b) A 15 m resolution pan-sharpened Landsat 7 false colour image on 18 February 2001 and (c) aspect of the study area around the Mindu landslide. The elevation data in a is a product of the NASA's Shuttle Radar Topography Mission (SRTM) and the aspect in c is a derivative of the DEM. The red polygons in b and c are the selected stable zone. Both the SRTM DEM in (a) and its derivative (c) are downloaded from the Geospatial Data Cloud website (<http://www.gscloud.cn/sources>). The Landsat image in b is a joint product of the USGS and NASA and was downloaded via the Google Earth Engine (GEE).

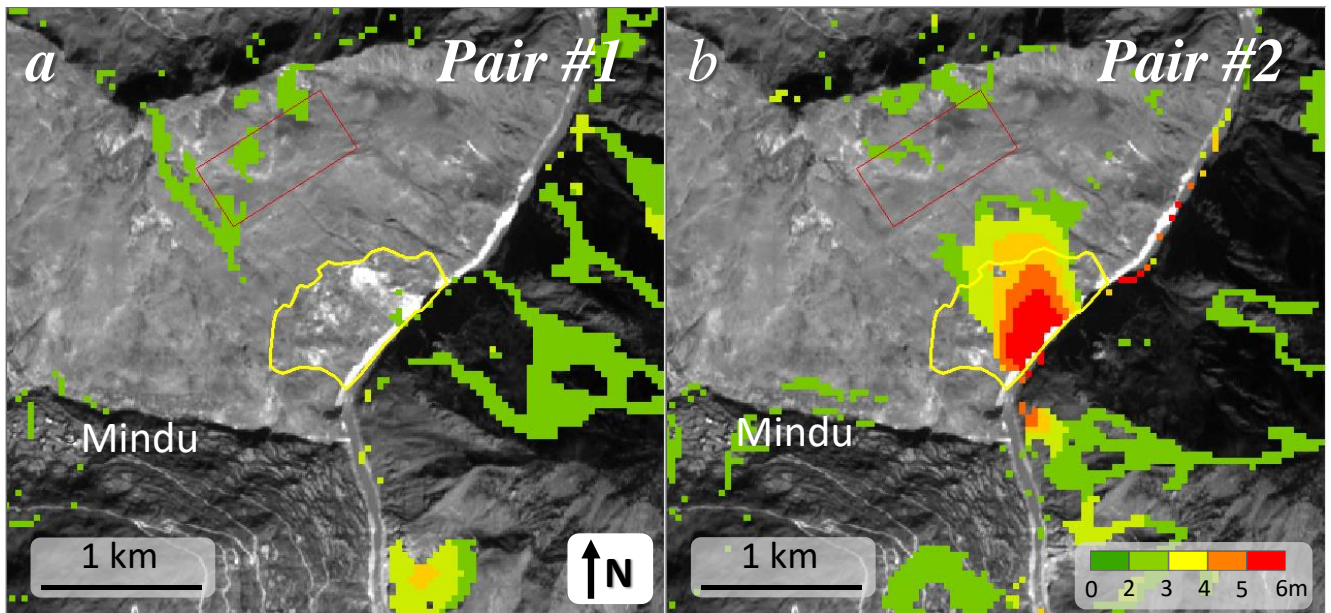


Figure 2: Detected slope displacements in image pair #1 and #2. Background Sentinel-2 images are acquired on 13 November 2015 and 12 November 2018, respectively. Both images were produced by the ESA's Sentinel-2 satellites and downloaded via the GEE.

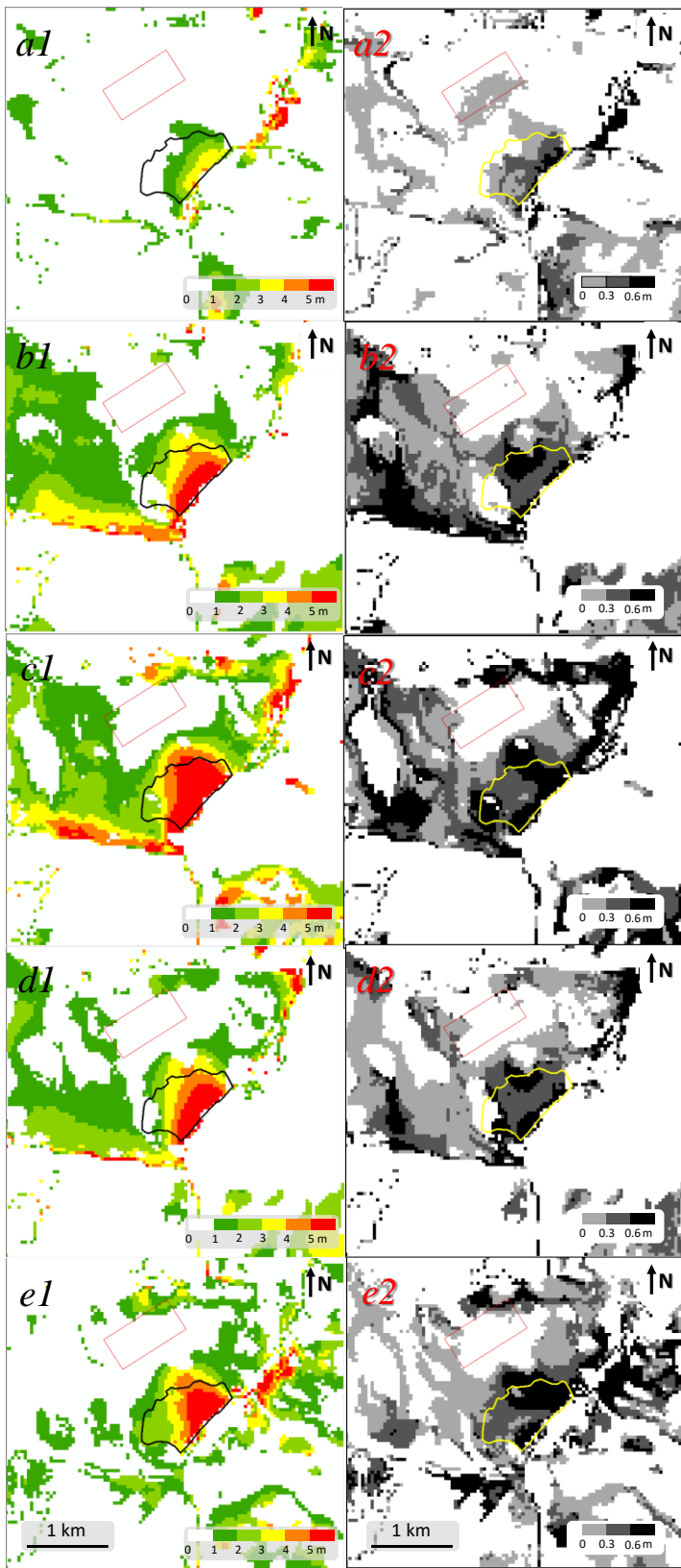


Figure 3: Means and standard deviations of the derived slope displacements in five targeted images (Tab. 1). Detected means and standard deviations of slope displacement on 13 Apr. 2019 (*a1*-*a2*), 17 Jul. 2019 (*b1*-*b2*), 24 Aug. 2019 (*c1*-*c2*), 5 Oct. 2019 (*d1*-*d2*), 12 Nov. 2019 (*e1*-*e2*), respectively.

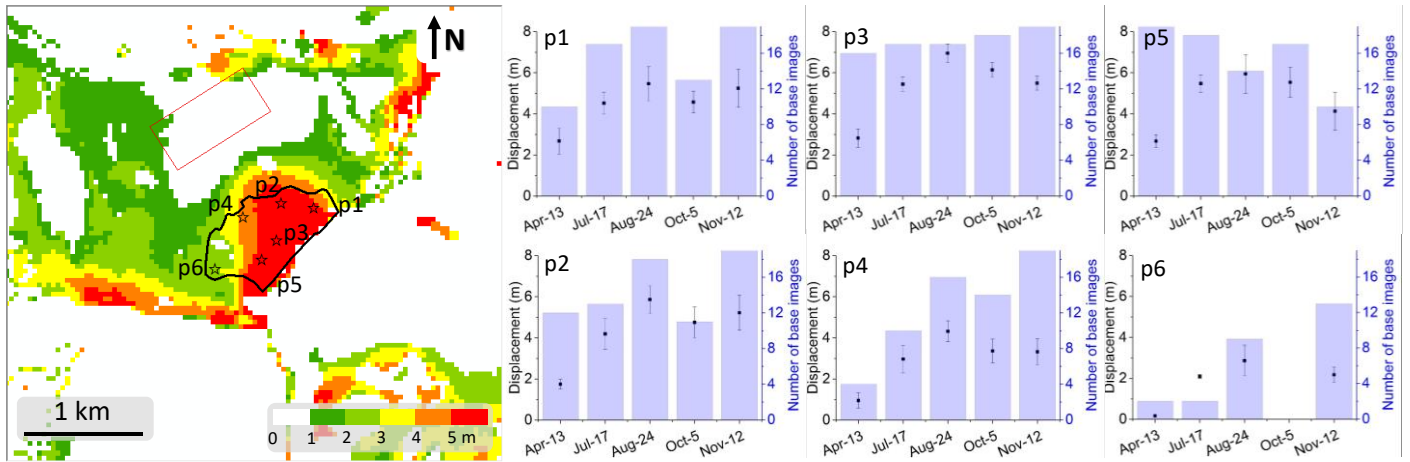


Figure 4: Time series of the slope displacements. Image to the left shows the slope displacements on 12 November 2019 and map colour is shown in minimum-maximum linear stretch type. Sub-panels p1-p6 to the right show means (points), standard deviations (vertical bars) and valid numbers (histograms) of cumulative displacements between the 19 base and 5 target images for the six selected points (stars) in the left image.

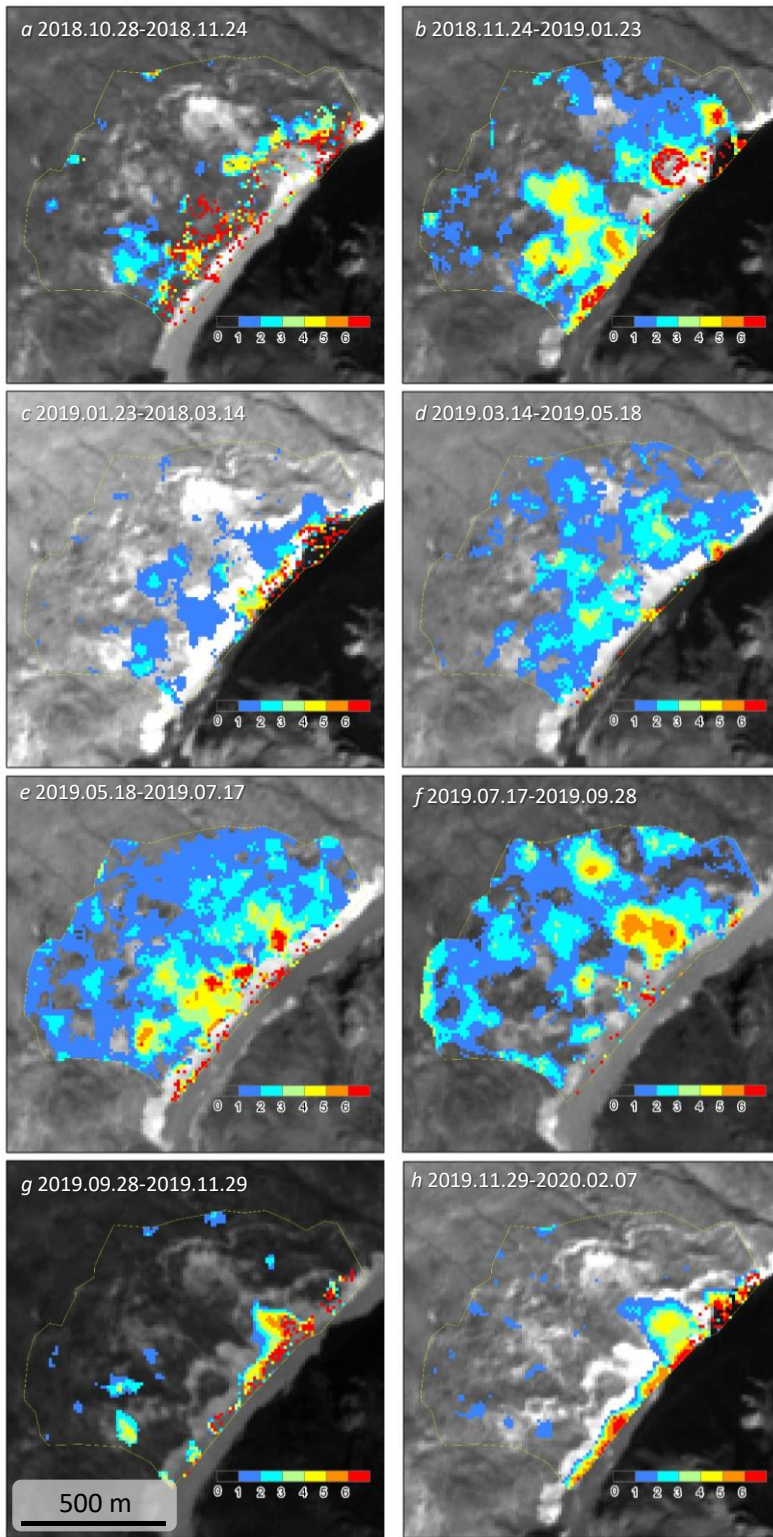


Figure 5: Slope displacements in different periods after the Baige floods (Background images are Sentinel-2 data produced by the ESA's Sentinel-2 satellites and downloaded via the GEE).

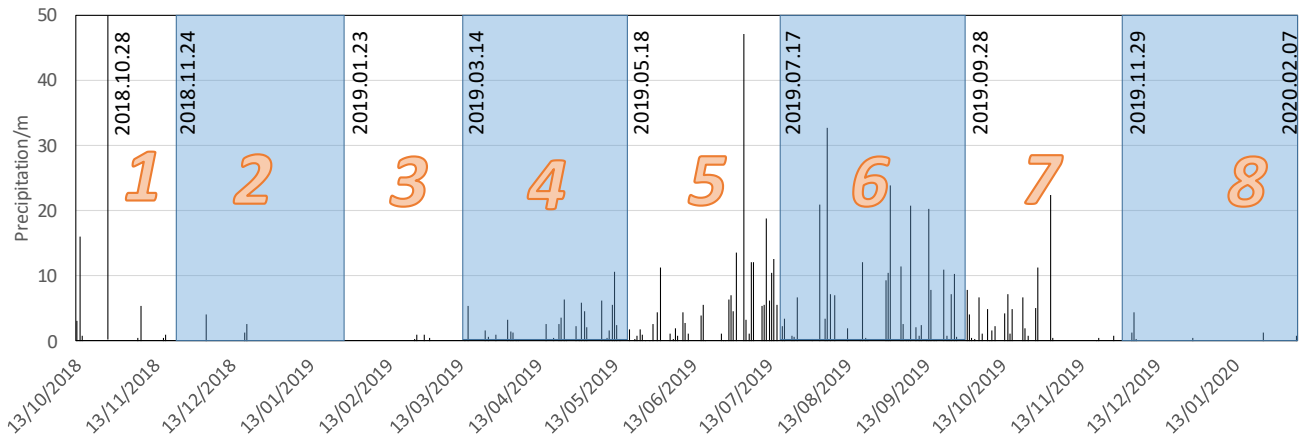


Figure 6: Daily precipitation of the Baiyu Meteorology station from October 2018 to February 2020.

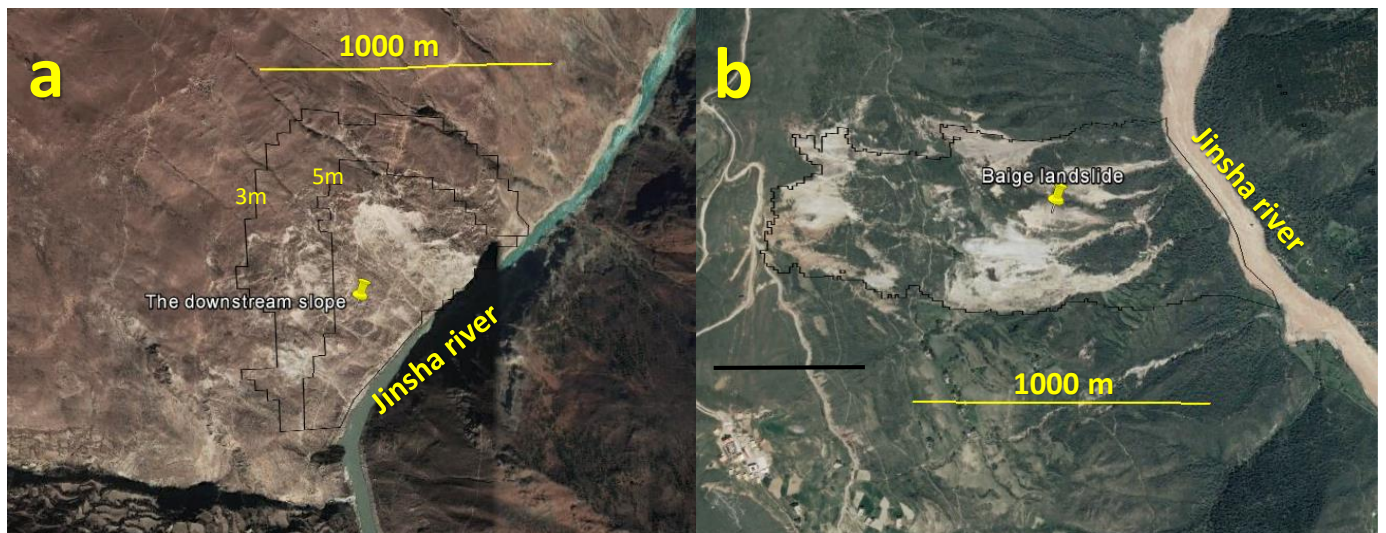


Figure 7: High spatial resolution images from the ©Google Earth. The image to the left is acquired on 30 March 2015 for the Mindu slope (a) and the right image is acquired on 18 July 2017 for the Baige slope (b).

350

Table 1. List of the 19 base images in early 2018 and 9 targeted images in 2019. Base images were used to detect cumulative slope displacements in targeted images. Image pairs used in this step are #3-#97.

19 base images in the stable period (in early 2018)	5 target images in the moving period (in 2019)
January: 11, 13, 16, 23, 28	
February: 5, 12, 17, 25	
March: 4, 9, 14, 19, 29	2019: 13-Apr., 17-Jul., 24-Aug., 5-
April: 3, 16, 23	Oct., 12-Nov.
May: 21	
June: 5	

355

Table 2. Eight periods (image pair #98-#105) were used to derive the Mindu slope movement.

Image pairs	Base image	Target image
#98	28 Oct. 2018	24 Nov. 2018
#99	24 Nov. 2018	23 Jan. 2019
#100	23 Jan. 2019	14 Mar. 2019
#101	14 Mar. 2019	18 May 2019
#102	18 May 2019	17 Jul. 2019
#103	17 Jul. 2019	28 Sep. 2019
#104	28 Sep. 2019	29 Nov. 2019
#105	29 Nov. 2019	07 Feb. 2020

Table 3. Detected image shifts (system error) in the “stable zone”. The EW-std and NS-std indicates uncertainties of the method and the EW-mean and NS-mean were used to derive the final displacements in image pair #1 and #2.

Image pairs	Dates	EW-mean	EW-std	NS-mean	NS-std	snr-mean	snr-std
#1	2015.11.13 2018.11.12	-0.495077	0.181026	-7.275188	0.253885	0.989819	0.001601
#2	2018.11.12 2019.11.12	4.115833	0.056559	9.914275	0.136149	0.989803	0.001434

360

365